Current Chemistry Letters 15 (2026) 545–558

Contents lists available at GrowingScience

Current Chemistry Letters

homepage: www.GrowingScience.com

Surface-engineered super-magnetic Fe_3O_4 nanocatalysts for efficient and recyclable synthesis of fentanyl citrate: An integrative experimental and theoretical framework

Seyyed Amir Siadati[a], Rezvan Yazdian-Robati[a*], Mohammad Ali Ebrahimzadeh[ab*] and Esmaeil Babanezhad[c]

[a]*Pharmaceutical Sciences Research Center, Hemoglobinopathy Institute, Mazandaran University of Medical Sciences, Sari, Iran*
[b]*Pharm. D., Ph.D. Professor of Medicinal Chemistry, Department of Medicinal Chemistry, The head Sari school of pharmacy, Sari, 4815733971, Iran*
[c]*Department of Environmental Health, Faculty of Health, Mazandaran University of Medical Sciences, Sari, Iran*

C H R O N I C L E

Article history:
Received January 24, 2026
Received in revised form
March 29, 2026
Accepted May 16, 2026
Available online
May 16, 2026

Keywords:
Fentanyl citrate
Total synthesis
Optimization
DFT
Weak interaction study

A B S T R A C T

In the present paper, the super-magnetic iron oxide nanoparticles (Fe_3O_4), functionalized with amine ($–NH_2$) and carboxyl (–COOH) groups were developed as efficient heterogeneous catalysts for synthesizing the fentanyl citrate compound. The structural analyses (FT-IR, SEM, TEM) have confirmed the successful surface modification while preserving particle morphology and magnetic behavior. The catalysts have exhibited excellent performance across key synthetic steps, enabling high yields under mild conditions and maintaining substantial activity after three consecutive cycles. The theoretical analyses, including RDG, NCI, ELF/LOL, and BCP evaluations, have revealed that reversible, weak noncovalent interactions dominate drug–salt adsorption, supporting the observed catalytic stability and easy magnetic recovery. Although relatively high catalyst loadings were required, this limitation was offset by reduced pH adjustments, the minimized phase contamination, and the potential for single-vessel operation. Overall, the combined experimental and theoretical findings demonstrate a practical, scalable, and mechanistically supported strategy for employing magnetic nano-sized catalysts in the pharmaceutical synthesis.

2026 by the authors; licensee Growing Science, Canada.

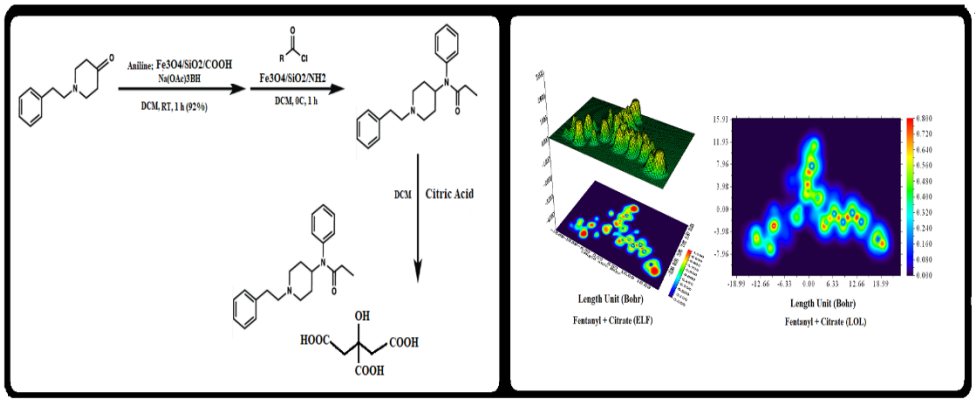

Graphical Abstract

1. Introduction

Selection of suitable intermediates has emerged as a pivotal structural unit in modern fentanyl synthesis, offering an ideal balance of reactivity and stability.[1-3] Since its initial utilization by Richter in 1970, [4] N-Phenethyl-4-piperidone (PPD) has enabled efficient construction of the N-phenethyl-N-propionamide framework, serving as a versatile precursor for laboratory and industrial syntheses of fentanyl and its related salts,[5–7] Early approaches, such as those reported by Gupta et

* Corresponding author
E-mail address Yazdian@mazums.ac.ir (R. Yazdian-Robati), MA.Ebrahimzadeh@mazums.ac.ir (M.A. Ebrahimzadeh)
© 2026 by the authors; licensee Growing Science, Canada
doi: 10.5267/j.ccl.2026.5.003

al.[8] and Valdez et al.[9] exploited selective reductive amination by $NaBH(OAc)_3$ to achieve high yields under mild and scalable conditions, demonstrating the potential of PPD-based methods for the practical pharmaceutical preparation.

Subsequent investigations explored alternative reducing agents, including $NaBH_4$, $NaBH(OAc)_3$, and combinations with molecular sieves, emphasizing precise moisture control and sequential reduction steps to optimize yields. For example, Kanamori et al.[10] achieved to 75–95% yields by careful reaction management, while Walz and Hsu[11] proposed a simplified $NaBH_4$/DCM protocol with 85% yield at ambient temperature. Robertson et al.[12] introduced a practical two-step process using $NaBH(OAc)_3$ and triethylamine (Et_3N), yielding 91% and 33%, suitable for a mid-scale production. More recent innovations have focused on green and scalable methodologies. Braga et al.[13] developed a visible-light photocatalytic continuous-flow system employing $[Ru(bpy)_3]Cl_2$ and ascorbic acid, reaching stepwise yields of 84% and 92%. These approaches combine high safety, reproducibility, and environmental compatibility, demonstrating the potential of modern catalysis to enhance efficiency in API synthesis[14,15] The ongoing development of new synthetic routes for active pharmaceutical ingredients (APIs) is critical for bridging laboratory optimization with industrial feasibility.[16-19] Robust, high-yielding, and reproducible methods, reduce cost, simplify operations, and improve safety in manufacturing. PPD-based strategies, especially when integrated with advanced catalysts or functionalized nanomaterials, provide a versatile platform for scalable fentanyl production and highlight the broader importance of innovative approaches in medicinal chemistry.

Computational methods increasingly support synthetic drug development by clarifying reaction pathways, estimating activation energies, and predicting catalyst or solvent effects. These tools help identify the most favorable reaction routes, minimize side reactions, and guide the rational selection and reaction conditions.[20-22] As a result, mechanistic modeling accelerates optimization and reduces the experimental trial-and-error typically required in organic chemistry.[23,24] Alongside these insights, industrial optimization principles such as heat-transfer management, solvent compatibility, moisture control, and reproducible mixing enable reliable scale-up of laboratory procedures.[25-27]

In this study, we have combined these computational evaluations (for stability and weak interaction studies of two fentanyl salts) with practical guidelines to refine the PPD-based synthesis. This integrated strategy improved operational safety, providing a streamlined and scalable workflow suitable for both research laboratories and pharmaceutical manufacturing.

2. Materials and Methods

2.1. Materials and Instruments

All chemicals were prepared from commercial sources and used without further purification. Superparamagnetic iron oxide nanoparticles (Fe_3O_4) were synthesized and functionalized as described below. Characterization of the nanoparticles was performed using Fourier-transform infrared (FTIR) spectroscopy on a PerkinElmer Spectrum RX I instrument. Morphological analysis was performed with the field emission scanning electron microscopy (FESEM, TESCAN MIRA 3) and transmission electron microscopy (TEM, ZEISS). Nuclear magnetic resonance (NMR) spectra were recorded using a Bruker Avance-400 spectrometer. Superparamagnetic nanoparticles were collected using high-strength neodymium magnets (≥1 T). All reactions were carried out under controlled temperature conditions and monitored using thin-layer chromatography (TLC) where appropriate. Moreover, the solvents were analytical grade, and all glassware was cleaned and dried prior to use.

2.2. Synthesis of Acidic and Basic Superparamagnetic Iron Oxide Nanoparticles (Fe_3O_4@SiO_2@NH_2 and Fe_3O_4@SiO_2@COOH)

As shown in **Fig. 1**, the Superparamagnetic Fe_3O_4 nanoparticles were synthesized by co-precipitation using $FeCl_3 \cdot 6H_2O$ (32 g) and $FeCl_2 \cdot 4H_2O$ (12 g) in a 2:1 molar ratio under N_2, followed by addition of 30% NH_4OH to form SMNPs.[28] Silica coating was achieved via the Stöber method, dispersing 20 g Fe_3O_4 in ethanol and adding 10 mL TEOS dropwise to obtain Fe_3O_4@SiO_2.[29] Also, amination was performed by reacting 20 g Fe_3O_4@SiO_2 with APTES in ethanol at 65 °C.[30] Finally, carboxylation used glutaraldehyde and subsequent H_2O_2 oxidation, yielding Fe_3O_4@SiO_2@COOH nanoparticles.[31]

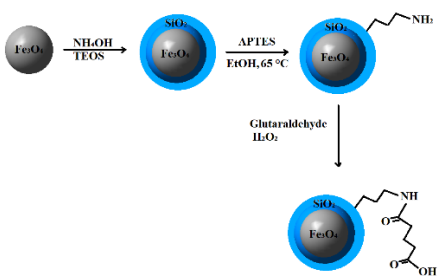

Fig. 1. Schematic illustration of the synthesis of superparamagnetic iron oxide nanoparticles (Fe_3O_4) functionalized with basic (–NH_2) and acidic (–COOH) surface groups.

2.3. Optimized Procedure for the Synthesis of Fentanyl Citrate

Initially, 330.0 mg of 1-Phenethyl-piperidin-4-one was dissolved in 3.5 mL of dichloromethane. Subsequently, 190.0 mg of aniline and 100.0 mg of carboxyl-functionalized superparamagnetic Fe_3O_4@SiO_2@COOH nanoparticles were added to the reaction flask. Next, 830.0 mg of sodium triacetoxyborohydride was introduced, and the reaction mixture was stirred at ambient temperature for 15 hours. The nanoparticles were then removed using a strong neodymium magnet.

To the collected mixture, 2.5 mL of water was added, and the temperature was maintained at 25 °C. The pH of the aqueous solution was adjusted to 7–8 using 30% sodium hydroxide, and the organic phase was separated. The dichloromethane phase was dried over 150.0 mg of anhydrous sodium sulfate and filtered. This dried organic phase was transferred to a new reaction vessel, and 40 wt% (130 mg) of amine-functionalized superparamagnetic Fe_3O_4@SiO_2@NH_2 nanoparticles was added. The system temperature was then lowered to 0–5 °C.

Subsequently, 320 mg of propionyl chloride and 3 mL of dichloromethane were added. The propionyl chloride solution was gradually dropped into the reaction mixture over 15 minutes. The reaction was stirred at 40 °C for 90 minutes, after which the nanoparticles were removed magnetically. The temperature was then reduced below 0 °C, 1.5 mL of n-hexane was added, and the mixture was stirred for an additional 1.5 hours. The precipitate was filtered, washed with 3 mL of hexane, dried, and weighed. Under optimized conditions, the isolated bis-fentanyl intermediate weighed 505 mg, corresponding to a 95.9% yield for this step and an overall two-step yield of 92.4%. The melting point was 87.5 °C.

For the citration step, 50.0 mg of the bis-fentanyl intermediate was dissolved in 1.5 mL of dichloromethane. Solid citric acid (37.1 mg) was gradually added to the solution until complete dissolution was achieved. The reaction mixture was heated to about 40 °C and stirred for 30 minutes, then cooled to 20–25 °C and stirred for an additional 1 hour. The resulting precipitate was filtered, washed with warm acetone, and dried. Under these optimized conditions, the fentanyl citrate precipitate weighed 74.0 mg, with a 94% yield. The melting point was 153–155 °C, and the overall yield of the entire synthesis was 86.9% (**Fig. 2**).

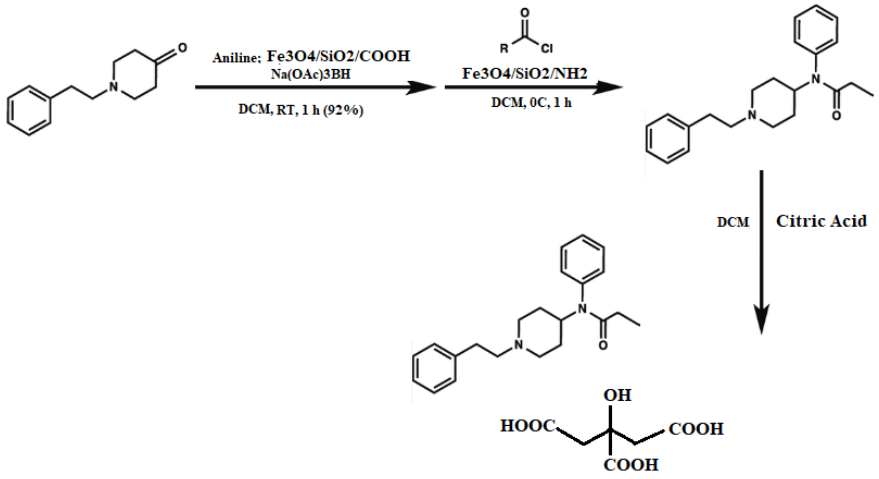

Fig. 2. The total synthesis of fentanyl citrate based on high amounts of acid and amine functionalized super magnetic nano particles

Fentanyl Citrate: 2-hydroxypropane-1,2,3-tricarboxylic acid; N-phenyl-N-[1-(2-phenylethyl)piperidin-4-yl]propanamide, Yield: 86.9%; 153-155 ° C;[32] ^{1}H NMR (400 MHz, DMSO-d_6) δ 7.56 – 7.38 (m, 3H), 7.38 – 7.05 (m, 7H), 4.66 (tt, J = 12.4, 3.8 Hz, 1H), 3.37 (d, J = 11.8 Hz, 2H), 2.97 (dd, J = 10.7, 5.9 Hz, 2H), 2.84 (dd, J = 6.9, 3.4 Hz, 2H), 2.82 – 2.71 (m, 2H), 2.59 (d, J = 15.2 Hz, 2H), 2.54 (s, 2H), 2.50 (d, J = 2.1 Hz, 1H), 1.94 – 1.85 (m, 2H), 1.82 (t, J = 7.4 Hz, 2H), 1.43 (qd, J = 13.1, 3.8 Hz, 2H), 0.88 (t, J = 7.4 Hz, 3H);[33] ^{13}C NMR (101 MHz, DMSO) δ 176.95, 172.49, 171.85, 138.75, 138.39, 130.89, 129.91, 129.12, 128.98, 128.91, 126.99, 72.02, 57.73, 51.91, 50.04, 44.38, 31.02, 28.48, 28.24, 9.90;[34] FTIR, KBr: 3855–3422 (O–H, N–H); 2943 (C–H); 1720 (C=O); 1642 (C=C); 1586 (C=C); 1280 (C–N, C–O, C–H bend); 1235 cm^{-1} (C–N, C–O, C–H bend);[35] MS: m/z: 337.1 (Fentanyl) $[M]^+$.[36]

The ^{1}H NMR spectrum of Fentanyl Citrate in DMSO-d_6 shows characteristic aromatic proton signals between 7.05-7.56 ppm (10H for two phenyl rings), with the methine proton of the piperidine ring appearing at 4.66 ppm (tt, 1H). Aliphatic protons from the piperidine ring, phenylethyl group, and propanamide moiety are observed in the region of 0.88-3.37 ppm, including the distinctive methyl triplet at 0.88 ppm (3H) and methylene protons of the citrate counterion at 2.54 ppm (s, 2H) and 2.59 ppm (d, 2H), confirming the presence and structure of both components.

The ^{13}C NMR spectrum of Fentanyl Citrate in DMSO reveals characteristic carbonyl carbons at 171.85-176.95 ppm, corresponding to the amide and citrate carboxylic acids, alongside eight distinct aromatic carbon signals between 126.99-138.75 ppm from the fentanyl moiety. Key aliphatic carbon signals include the piperidine CH at 57.73 ppm, methylene carbons of the phenylethyl and piperidine rings (28.24-51.91 ppm), the citrate CH_2 at 44.38 ppm, and the terminal methyl carbon of the propanamide group at 9.90 ppm, affirming the compound's structural integrity.

2.4. Computational details

Several initial geometries were generated for each sorbent salt–drug system, and all structures were optimized to determine the most stable configurations. Before evaluating interactions, the isolated salts and free fentanyl molecule were fully optimized to obtain their minimum-energy structures. All quantum-chemical calculations were carried out using the Gaussian package[37] at the B3LYP/6-311G(d,p) level of theory,[38,39] a widely applied method in adsorption and interaction studies.[40,41] Gas-phase conditions were selected to probe intrinsic drug–salt binding.

The adsorption energy (E_{ads}) was calculated using:

$$E_{ads}=E_{sys}-(E_{salt}+E_{FNC}) \quad (1)$$

where E_{sys}, E_{salt}, and E_{FNC} correspond to the energies of the complex, isolated salt, and isolated fentanyl, respectively. Recovery time (τ) was obtained from Eq. (2):[42]

$$\tau = \upsilon^{-1}\exp(-E_{ads}/K_bT) \quad (2)$$

Noncovalent interaction (NCI) analysis was performed using RDG descriptors in Multiwfn 3.7,[43] with scatter plots generated in Gnuplot 5.7[44] and RDG isosurfaces visualized in VMD.[45] Complementary ELF and LOL calculations were also carried out to characterize electron localization and weak intermolecular interactions within the adsorption complexes.

3. Results and discussions

3.1. Characterization of Acidic and Basic Superparamagnetic Iron Oxide Nanoparticles (Fe_3O_4@SiO_2@NH_2 and Fe_3O_4@SiO_2@COOH)

In this stage of the project, superparamagnetic iron oxide nanoparticles were synthesized as the core material (**Fig. 1**) and subsequently functionalized to enhance colloidal stability and provide reactive surface groups. The nanoparticles were sequentially coated with silica, followed by amine and carboxylic acid functionalization. Amino-functionalization introduced –NH_2 groups, was used as a mild basic catalyst, whereas carboxylic acid was applied as a mild basic catalyst.

3.1.1. FT-IR Spectroscopy

FTIR spectra of the Fe_3O_4 nanoparticles show a characteristic absorption band at approximately 579 cm^{-1}, corresponding to the stretching vibration of the Fe-O bond, indicative of the spinel structure of magnetite. Following the surface functionalization with amino groups (Fe_3O_4-NH_2), spectral changes were observed in the regions 3200–3400 cm^{-1} (-NH and -OH stretching vibrations) and 1560–1650 cm^{-1} (N–H bending vibration), confirming the presence of amino functionalities. In the final stage, after modification with carboxylic acid groups (Fe_3O_4-COOH), a band appeared around 1700–1730 cm^{-1}, corresponding to C=O stretching, along with increased intensity of hydroxyl bands. Although these spectral changes are relatively subtle and some bands may be difficult to resolve due to overlapping or signal attenuation, the overall shifts and intensity variations provide supporting evidence for successful surface functionalization of nano-sized composites.[46-50]

3.1.2. The SEM and TEM analysis further complements the FTIR data

The SEM and TEM images reveal that the Fe_3O_4 nanoparticles exist as spherical aggregates, and surface functionalization does not significantly alter the overall morphology (**Fig. 3** and **Fig. 4**). It should be noted that surface chemical modifications, such as the introduction of –NH_2 or –COOH groups, are not directly observable in SEM; only the preservation of particle morphology and distribution can be assessed.

Therefore, the combined analysis of FTIR, TEM and SEM confirms that surface functionalization of the nanoparticles has been successfully achieved, even though spectral and imaging evidence individually may have limitations in resolution.

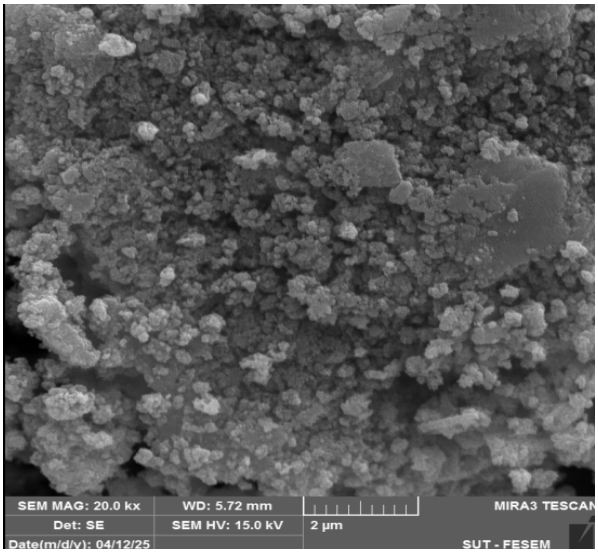

Fig. 3. SEM image of superparamagnetic iron oxide nanoparticles functionalized with acidic groups (Fe_3O_4@SiO_2@COOH).

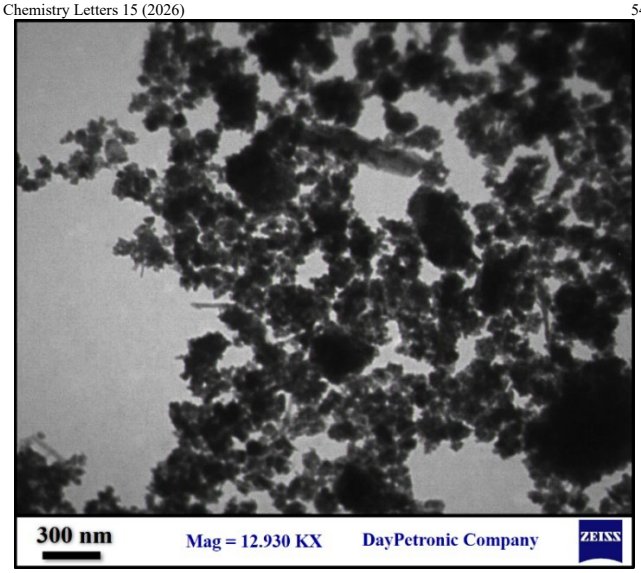

Fig. 4. TEM image of superparamagnetic iron oxide nanoparticles functionalized with acidic groups (Fe_3O_4@SiO_2@COOH).

3.1.3. Recyclability of Superparamagnetic Acidic and Basic Iron Oxide Nanoparticles (Fe_3O_4@SiO_2@NH_2 and Fe_3O_4@SiO_2@COOH)

To evaluate the reusability of the acidic and basic superparamagnetic iron oxide catalysts, each catalyst was recovered after completion of the reaction using a neodymium magnet and washed with the corresponding reaction solvent. The recovered catalysts were subsequently dried under vacuum at 50 °C for 24 h and then ground to a fine powder. As summarized in **Table 1**, the catalytic activity of both Fe_3O_4@SiO_2@COOH and Fe_3O_4@SiO_2@NH_2 remained substantially high even after three consecutive reaction cycles, indicating minimal loss of activity upon reuse.

Table 1. Effect of recycling on the catalytic activity of acidic and basic superparamagnetic iron oxide nanoparticles.

Entry	Catalyst Type	Recycling Cycle	Reaction Yield (%)
1	Fe_3O_4@SiO_2@COOH	0	96.3
2	Fe_3O_4@SiO_2@COOH	1	84.1
3	Fe_3O_4@SiO_2@COOH	2	79.4
4	Fe_3O_4@SiO_2@NH_2	0	95.9
5	Fe_3O_4@SiO_2@NH_2	1	87.2
6	Fe_3O_4@SiO_2@NH_2	2	81.5

These results confirm the excellent recyclability and stability of the functionalized superparamagnetic nanoparticles under the applied reaction conditions.

3.2. Optimization of the fentanyl citrate synthesis

3.2.1. Optimization of the First Step of Fentanyl Synthesis (Condensation of 1-Phenethyl-piperidin-4-one with Aniline)

To optimize the condensation of aniline with 1-phenethyl-piperidin-4-one followed by in situ reduction of the imine intermediate (**Fig. 2**), initial experiments were performed using acetic acid as the acid catalyst and $NaBH_4$ as the reducing agent in protic media, including water and lower alcohols. Preliminary results indicated that the reaction proceeded very slowly in water, giving only a faint product trace on TLC even after 24 h, accompanied by a low isolated yield. Methanol and ethanol afforded slightly better conversion; however, after 24 h, the product spots on TLC remained weaker than those corresponding to the limiting reagent (1-phenethyl-piperidin-4-one). Work-up of these reactions resulted in a viscous, paste-like crude material with poor yields.

Using toluene as the solvent, in combination with p-toluenesulfonic acid and $NaBH(OAc)_3$, improved performance was observed. Refluxing for approximately 30 h afforded the desired product in 84.2% yield. Despite this improvement, the product was still semi-solid, and the requirement of prolonged heating at ~110 °C raised concerns regarding the economic feasibility and scalability of this route. Experiments 5–7 demonstrated that the DCM–acetic acid system in the presence of $NaBH(OAc)_3$ significantly outperformed $NaBH_4$, delivering approximately 30% higher yield under otherwise identical conditions. In addition, dichloromethane consistently provided better reaction progress than protic solvents. Increasing the reaction temperature from 25 °C to 40 °C resulted in a further 13% increase in yield.

Additional solvent systems including ethyl acetate–acetic acid, acetonitrile–acetic acid, and hexane–acetic acid were also evaluated with $NaBH(OAc)_3$. Hexane proved unsuitable, as both reaction rate and TLC conversion were negligible. Ethyl acetate afforded a yield approximately 10% lower than the corresponding DCM reaction. Acetonitrile showed a higher reaction rate, producing yields roughly 5% greater than DCM; however, efficient conversion required elevated temperatures near 80 °C, reducing its practicality.

Based on the superior balance of conversion, yield, and operational simplicity, DCM and $NaBH(OAc)_3$ were selected as the optimal solvent–reductant system for subsequent investigations. The next phase evaluated the use of the surface-acid-modified superparamagnetic catalyst $Fe_3O_4@SiO_2@COOH$. At 25 °C, employing 20 wt% of this catalyst afforded a yield of approximately 91%. Increasing catalyst loading to 30 wt% under identical conditions raised the yield to 96.3%. Further increasing the reaction temperature from 25 °C to 40 °C produced no meaningful improvement, indicating that the reaction is not strongly temperature-dependent within this range.

Table 2. The First Step of Fentanyl Synthesis (Condensation of 1-Phenethyl-piperidin-4-one with Aniline)

Entry	Acid Catalyst (Amount)	Hydride Source	Solvent	Time (h)	Temp (°C)	Yield (%)
1	Acetic acid (1 equiv.)	$NaBH_4$	Water	30	100	Very low
2	Acetic acid (1 equiv.)	$NaBH_4$	Methanol	30	60	37.5
3	Acetic acid (1 equiv.)	$NaBH_4$	Ethanol	30	70	43.0
4	p-Toluenesulfonic acid (5 wt%)	$NaBH(OAc)_3$	Dry toluene	30	110	84.2
5	Acetic acid (1 equiv.)	$NaBH(OAc)_3$	Dichloromethane	15	25	85.2
6	Acetic acid (1 equiv.)	$NaBH_4$	Dichloromethane	15	25	54.1
7	Acetic acid (1 equiv.)	$NaBH_4$	Dichloromethane	15	40	67.5
8	$Fe_3O_4@SiO_2@COOH$ (20 wt%)	$NaBH(OAc)_3$	Dichloromethane	15	25	91.4
9	$Fe_3O_4@SiO_2@COOH$ (30 wt%)	$NaBH(OAc)_3$	Dichloromethane	15	25	96.3
10	$Fe_3O_4@SiO_2@COOH$ (30 wt%)	$NaBH(OAc)_3$	Dichloromethane	15	40	96.8
11	Acetic acid (1 equiv.)	$NaBH(OAc)_3$	Ethyl acetate	15	78	75.3
12	Acetic acid (1 equiv.)	$NaBH(OAc)_3$	Acetonitrile	15	82	90.7
13	Acetic acid (1 equiv.)	$NaBH(OAc)_3$	Hexane	15	70	<5 (trace)

Consequently, the optimized conditions were established as: DCM as solvent, $NaBH(OAc)_3$ as the reductant, and 30 wt% COOH-functionalized $Fe_3O_4@SiO_2$ as the heterogeneous acid catalyst (Table 2).

3.2.2. Optimization of the Acylation Step: Reaction of (1-Phenethyl-piperidin-4-yl)-phenylamine with Propionyl Chloride

The acylation of the intermediate (1-Phenethyl-piperidin-4-yl)-phenylamine with propionyl chloride was first examined under solvent-free conditions. Preliminary experiments indicated that performing the reaction in the absence of solvent significantly enhanced the conversion and final yield, mainly due to the high reactivity of propionyl chloride. However, the solvent-free protocol demanded the use of more than 20 molar equivalents of propionyl chloride to achieve meaningful progress. Despite the increased yield, this approach is neither cost-effective nor operationally practical, given the high price**,** lacrimatory nature**,** and strong irritant odor of propionyl chloride. Furthermore, when no base was used, the reaction proceeded very slowly, giving only a faint product spot on TLC, confirming that the presence of a base is essential for efficient acylation. Comparison of bases showed that inorganic bases (e.g., $CaCO_3$) led to slower reaction rates and lower yields relative to liquid organic bases such as triethylamine (see **Table 3**).

Table 3. Optimization of the Acylation Reaction Between (1-Phenethyl-piperidin-4-yl)-phenylamine and Propionyl Chloride

Entry	Type and Ratio of Base Catalyst	Equivalents of Propionyl Chloride	Solvent	Time (h)	Temperature (°C)	Yield (%)
1	Triethylamine (1:1 molar ratio)	25	–	2	25–40	97.1
2	Sodium carbonate (1:1 molar ratio)	25	–	2	25–40	85.5
3	–	25	–	2	25–40	–
4	$Fe_3O_4@SiO_2@NH_2$ (30 wt%)	25	–	2	25–40	88.3
5	$Fe_3O_4@SiO_2@NH_2$ (40 wt%)	25	–	2	25–40	93.6
6	$Fe_3O_4@SiO_2@NH_2$ (50 wt%)	25	–	2	25–40	94.0
7	$Fe_3O_4@SiO_2@NH_2$ (40 wt%)	1	Dichloromethane	2	20–40	91.5
8	$Fe_3O_4@SiO_2@NH_2$ (40 wt%)	1.5	Dichloromethane	2	20–40	95.9
9	$Fe_3O_4@SiO_2@NH_2$ (40 wt%)	2	Dichloromethane	2	20–40	62.2
10	$Fe_3O_4@SiO_2@NH_2$ (40 wt%)	1.5	Acetonitrile	2	20–40	89.6
11	$Fe_3O_4@SiO_2@NH_2$ (40 wt%)	1.5	Ethyl acetate	2	20–40	75.3

To optimize the catalytic basic conditions, $Fe_3O_4@SiO_2@NH_2$ nanoparticles were evaluated at loadings of 30, 40, and 50 wt% relative to the amine substrate. Increasing the catalyst loading from 30% to 40% resulted in an improvement of over 5% in product yield, while further increasing the loading to 50% provided no additional benefit. Thus, a 40 wt% catalyst loading was selected as the optimal ratio. Subsequently, DCM was introduced as the reaction solvent. Although the presence of solvent slightly decreased the reaction rate compared to the solvent-free protocol, the overall performance,

reproducibility, and operational manageability were superior. Moreover, using 1.5–2.0 equivalents of propionyl chloride enhanced the product yield; however, the difference between 1.5 and 2.0 equivalents was negligible. Therefore, 1.5 equivalent of Propionyl Chloride (2 h, 40w% catalyst) was adopted as the optimal molar ratio.

Other aprotic solvents, such as acetonitrile and ethyl acetate, were also tested. Both provided slightly lower yields than DCM under identical conditions. Predictably, due to the high reactivity and moisture sensitivity of propionyl chloride, protic or nucleophilic solvents (e.g., water, methanol, ethanol, 1-propanol, 1-butanol) were entirely unsuitable for this transformation.

3.2.3. Optimization of the Citrate addition Step to Produce Fentanyl Citrate

The standard procedure for the citrate addition of synthesized fentanyl base was optimized as follows. First, 50 mg of the crude fentanyl free base was dissolved in 1.5 mL dichloromethane. A stoichiometric amount of solid citric acid (relative to the base content) was then added gradually with gentle stirring until complete dissolution or near-dissolution occurred. The reaction mixture was subsequently heated to 40 °C and stirred for 30 min, followed by cooling to 20–25 °C and additional stirring for 1 h. The resulting precipitate was filtered, washed thoroughly with warm acetone, and dried to afford purified fentanyl citrate. The optimized procedure delivered 74 mg of product with a 93.5% yield, corresponding to an overall process yield of 86.3% (**Table 4**). The obtained material was characterized by ^{1}H NMR and ^{13}C NMR spectroscopy. The final product exhibited a melting point of 153–155 °C, consistent with reported values for fentanyl citrate.

Table 4. Citration Step in the Synthesis of Fentanyl Citrate

Entry	Time (h)	Temperature (°C)	Solvent	Molar Ratio of Citric Acid	Yield (%)
1	2	20–25	Methanol	1	76.3
2	2	25–40	Methanol	1	78.0
3	2	20–25	Ethanol	1	64.9
4	2	20–25	Isopropanol	1	60.4
5	1:30	25–40	Dichloromethane	1	83.1
6	2	25–40	Toluene	1	–
7	2	25–40	Ethyl acetate	1	53.7
8	2	25–40	Acetonitrile	1	77.9
9	1:30	25–40	Dichloromethane	1	87.5
10	1:30	25–40	Dichloromethane	1.3	93.5
11	1:30	25–40	Dichloromethane	1.5	92.8
12	1:30	20–25	Dichloromethane	1.3	88.1
13	1:30	40	Dichloromethane	1.3	93.1 (impure)
14	4	25–40	Dichloromethane	1.3	93.6

To optimize the citration reaction of fentanyl, the effects of solvent, temperature, reaction time, and molar ratios were systematically examined. For solvent screening, methanol, ethanol, isopropanol, toluene, ethyl acetate, and dichloromethane were evaluated. Among the tested alcohols, methanol provided the highest yield, whereas reactions conducted in toluene and ethyl acetate resulted in the lowest efficiencies; the reaction mixture in toluene formed a paste-like mass, and ethyl acetate afforded only 53.7% yield. Subsequently, acetonitrile was investigated and produced a moderate improvement, increasing the reaction yield to 77.9%. Overall, dichloromethane outperformed all other solvents, including acetonitrile, delivering a yield of 87.5%. Moreover, employing dichloromethane at this stage offers a strategic advantage by enabling a potential one-pot procedure for the entire total synthesis of fentanyl citrate. Therefore, dichloromethane was selected for further optimization. In experiments 9 and 10, increasing the molar ratio of citric acid to fentanyl to 1.3 and 1.5 equivalents improved the yields to 93.5% and 92.8%, respectively. Based on these results, a 1.3 molar ratio was selected as the optimal condition. Temperature variations were also assessed (experiments 11 and 12). Lowering the temperature to 20 °C resulted in a slight decrease in yield, whereas raising it to about 40 °C increased the formation of impurities, as confirmed by TLC analysis. Extending the reaction time from 90 minutes to 4 hours (experiment 13) produced no meaningful improvement (<1%) and led to the appearance of additional impurity spots in TLC. Accordingly, dichloromethane as solvent, a reaction temperature of 25–40 °C, a total reaction time of 90 minutes, and a 1.3 molar ratio of citric acid to fentanyl were established as the optimized conditions for the citration step.

3.3. Weak interaction studies and adsorptions energies

3.3.1. Geometrical optimizations and critical pint calculations

As given in **Table 5** and Fig. 5, the BCP/NCI maps and adsorption parameters clearly reveal that fentanyl interacts much more strongly with hydrochloric acid than with citric acid. The adsorption energy of the fentanyl HCl system (-2.36 kcal mol^{-1}) is nearly seven times larger in magnitude than that of fentanyl citrate (-0.30 kcal mol^{-1}), indicating a substantially stronger stabilizing interaction. This enhanced stability is fully supported by the topological data: the HCl system exhibits a prominent BCP with $\rho \approx 0.059$ a.u. and $V(r) \approx -0.058$ a.u., reflecting a highly localized electron density and a significantly more negative potential energy density relative to the citrate contacts. These values are characteristic of a strong hydrogen-bonding/ionic or partially covalent proton-transfer-like interaction. The experimentally consistent H···N distance of 1.12 Å

in the HCl complex further confirms formation of a tight ionic contact (protonated fentanyl · Cl^-), whereas the 2.02 Å H···N separation in the citric acid complex corresponds to a moderate, predominantly electrostatic hydrogen bond with weaker electron-density concentration.

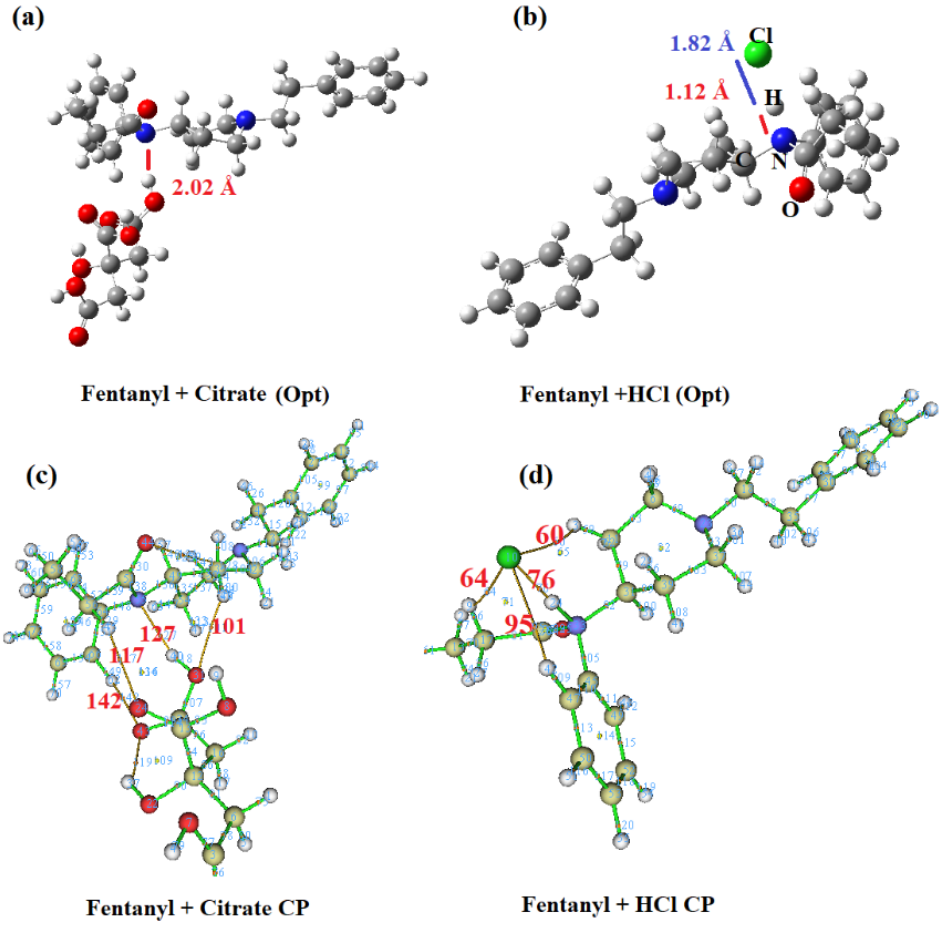

Fig. 5. The geometrical optimizations (a-b) and the Bond Critical Point maps (c-d) for each of the drug-salt adsorption system

The dynamic descriptors also align with this trend: the recovery time τ for the fentanyl–HCl system ($1.80(10^{-9})$ s) is one to two orders of magnitude greater than that of fentanyl–citrate ($5.54(10^{-11})$ s), indicating a more persistent adsorption state. The consistently positive Laplacian values ($\Delta^2\rho > 0$) alongside small but negative V(r) values in both systems classify the interactions as closed-shell, typical of hydrogen bonds and ionic contacts; however, the substantially higher ρ and more negative V(r) in the HCl complex suggest partial covalency and a deeper potential well. Collectively, the topological parameters, adsorption energies, and bond distances demonstrate that citric acid stabilizes fentanyl through weak, multipoint physisorption, whereas hydrochloric acid induces a strong protonation-driven ionic interaction, directly facilitating formation of the stable fentanyl hydrochloride salt.

Table 5. The Bond Critical Point parameters of the adsorption interactions which are in a. u. Also, the E_{ads} is in kcal mol^{-1} and the recovery time τ is in s.

System	E_{ads} (kcal mol^{-1})	Recovery time τ (s)	Interaction number	ρ (r)	$\Delta^2\rho$ (r)	V (r)
Fentanyl + Citrate	-0.30	$5.54(10^{-11})$	101	0.008	0.043	-0.006
			117	0.005	0.027	-0.002
			127	0.027	0.068	-0.024
			142	0.010	0.050	-0.007
Fentanyl + HCl	-2.36	$1.80(10^{-9})$	60	0.007	0.026	-0.004
			64	0.009	0.033	-0.005
			76	0.059	0.092	-0.058
			95	0.011	0.039	-0.006

3.3.2. LOL and ELF estimations

Fig. 6 represents the ELF maps for both systems reveal that salt formation reorganizes the electron density around the protonated site of fentanyl; however, the polarization pattern in the presence of citrate is significantly stronger and more spatially extended. In the fentanyl–citrate complex, high-ELF regions (0.65–0.80) spread around the citrate carboxylates and the protonated nitrogen of fentanyl, indicating multisite electrostatic stabilization, the formation of Lewis-type electron-rich pockets, and enhanced electron-pair localization. This multisite anchoring drives the geometry toward a lower-energy configuration and markedly increases the stability of the salt. In contrast, the ELF distribution in the fentanyl–HCl system shows a single, linear protonated region with moderate localization (0.40–0.55), characteristic of simple N–H^+ ionization without extended cooperative interactions. Thus, while HCl induces only a classical single-site protonation, citric acid establishes a multi-centered electronic locking mechanism that stabilizes the complex more effectively.

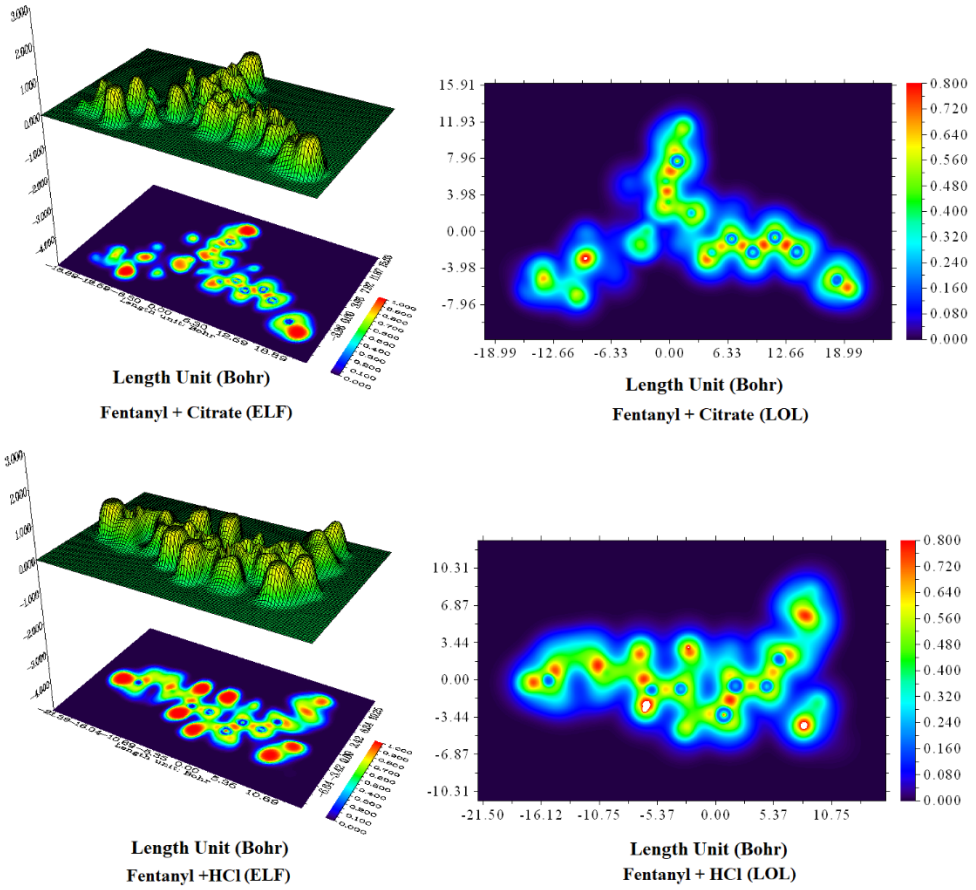

Fig. 6. ELF and LOL maps representing the orbital interactions and charge transfer pathways in salt–drug complexes, highlighting covalent versus ionic binding.

The LOL maps further support this behavior: in the fentanyl–citrate complex, the local electron-flow channels are highly dispersed and form multiple yellow–red loops, indicating steep local gradients, continuous density pathways, and enhanced delocalization across the interacting sites. This pattern demonstrates that citrate not only donates the proton but also creates several auxiliary density-transfer channels through its carboxylate groups, thereby increasing adsorption energy and stabilizing charge separation within the structure. Conversely, the LOL pattern of the fentanyl-HCl salt is much simpler and nearly linear, exhibiting only a few localized peaks around the N–H^+ region reflecting restricted delocalization and the absence of reinforcing density pathways. Together, the ELF and LOL analyses confirm that citrate produces an extended, multipolar interaction network, whereas HCl provides only a single-point protonation site, explaining the higher adsorption strength and improved thermodynamic stability of fentanyl in the citrate form. Notably, the higher adsorption energy observed with HCl arises from semi-covalent N···H bonding, reflecting the stronger acidity of HCl compared to citric acid, which accounts for the more intense protonation-driven stabilization in the HCl salt.

3.3.3. RDG and NCI calculations

Fig. 7 shows the RDG isosurfaces for the fentanyl citrate and fentanyl HCl systems which reveal distinct noncovalent interaction patterns that directly correlate with their salt-formation behavior. In the citrate complex, the RDG minima coincide with broad, low-density regions around the protonated tertiary amine of fentanyl and the multiple carboxylate oxygens of citric acid, indicating strong electrostatic attraction accompanied by secondary hydrogen-bond–assisted stabilization. The more extended green-turquoise RDG domains suggest a distributed network of weak-to-moderate interactions that collectively increase the stability and rigidity of the ion pair. Conversely, the fentanyl HCl system shows a sharper, more localized RDG well corresponding to the Coulombic bond between protonated fentanyl and chloride, reflecting a simpler and more compact binding motif dominated by a single strong ionic contact. The NCI plots further differentiate the interaction landscapes of the two salts. In the citrate salt, the large, diffuse green NCI patches around the fentanyl citrate interface denote an ensemble of stabilizing noncovalent forces electrostatic, hydrogen bonding, and van der Waals producing a more complex and cooperative binding topology. Blue-tinged regions indicate zones of stronger attraction, consistent with the tri-carboxylate architecture of citrate engaging the cationic fentanyl through multipoint anchoring. In contrast, the fentanyl HCl NCI map exhibits a concentrated blue region adjacent to the chloride, characteristic of a dominant ionic pair with minimal auxiliary interactions. This comparative analysis highlights that citrate forms a more multi-dimensional and robust interaction network, while HCl forms a highly localized but intense ionic bond, fully consistent with their differing physicochemical stability and salt behavior. Importantly, the higher adsorption energy observed in the HCl complex arises from semi-covalent N···H bonding, reflecting the stronger acidity of HCl compared to citric acid and explaining the enhanced protonation-driven stabilization despite the simpler, localized binding pattern.

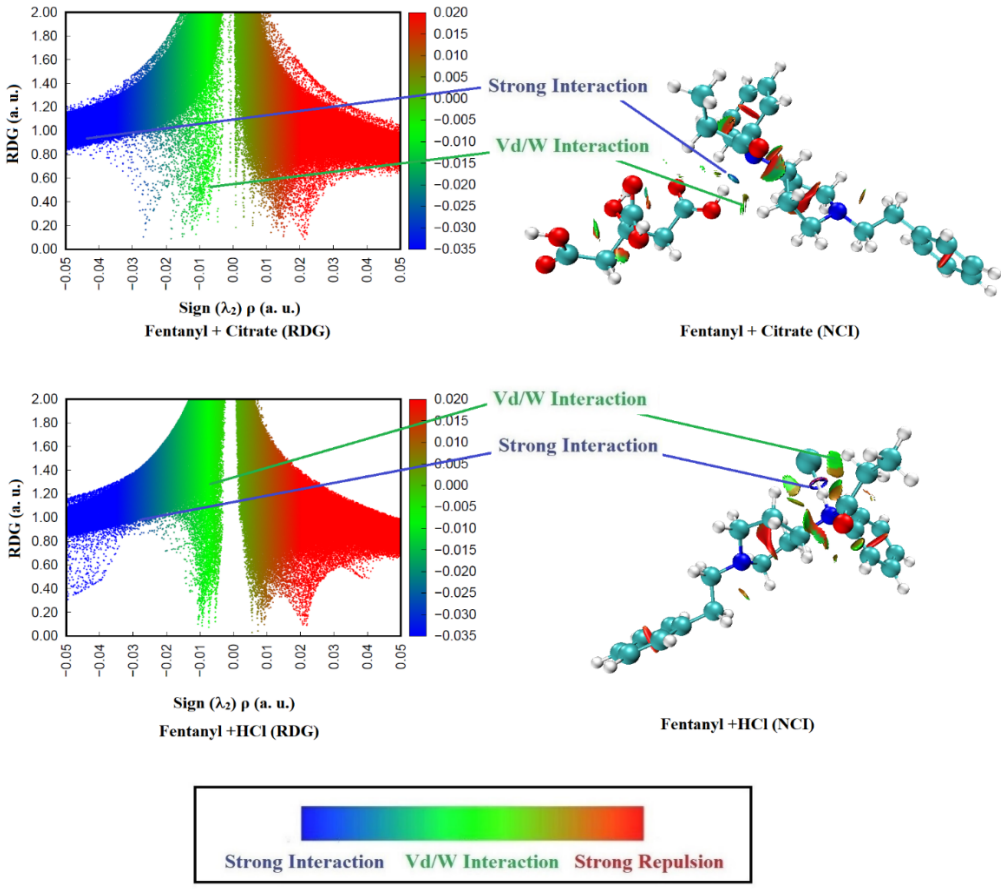

Fig. 7. Reduced density gradient (RDG) scatter plots and non-covalent interaction (NCI) plots for adsorption of each drug by the acid salt

3.4. Integrative discussions

The integration of the experimental optimization studies with the structural and mechanistic insights obtained from characterization collectively demonstrates a coherent and efficient pathway for the synthesis of fentanyl citrate using recyclable acidic and basic superparamagnetic iron oxide nanocatalysts. The FTIR, SEM, and TEM analyses confirmed successful functionalization of Fe_3O_4@SiO_2@NH_2 and Fe_3O_4@SiO_2@COOH without altering particle morphology, validating their suitability as heterogeneous catalytic sites. These structural features directly correlate with the superior

catalytic behavior observed in the key steps of synthesis. In the first condensation–reduction step, the COOH-functionalized nanoparticles significantly enhanced both conversion and yield, outperforming classical homogeneous acids and enabling high selectivity under mild conditions. The mechanistic advantage likely arises from localized acid-site accessibility and reduced proton diffusion barriers on the nanoparticle surface. Similarly, in the acylation step, the NH_2-functionalized catalyst provided an efficient heterogeneous base environment, enabling clean activation of propionyl chloride and stabilizing the amide-forming transition state, while avoiding the drawbacks of excess corrosive reagents or volatile liquid bases. The recyclability data further confirm the structural robustness of both catalysts, maintaining high catalytic output after multiple cycles. Finally, the citration step benefited from insights gained earlier regarding solvent polarity, thermal stability, and acid–base pairing: dichloromethane served as an optimal medium not only for salt formation but also as a unifying solvent that enables a potential one-pot synthetic integration. Overall, aligning catalyst design with mechanistic demands across all stages resulted in a streamlined, high-yielding pathway where experimental outcomes and theoretical justification mutually reinforce the efficiency, selectivity, and scalability of the process.

4. Conclusion

In conclusion, superparamagnetic iron oxide nanoparticles (Fe_3O_4) were successfully synthesized and surface-functionalized with amine (–NH_2) and carboxyl (–COOH) groups, enabling their application as efficient and reusable heterogeneous catalysts in the synthesis of fentanyl citrate. FT-IR, SEM, and TEM analyses have confirmed that the functionalization occurred without compromising particle morphology or magnetic responsiveness. The recyclability tests demonstrated minimal loss in catalytic performance over three consecutive cycles, underscoring the structural stability and chemical resilience of both acidic and basic nanocatalysts under the reaction conditions. These experimental observations are strongly supported by the theoretical results: RDG, NCI, ELF/LOL, and BCP analyses revealed that the drug–salt interactions with functional groups occur through the weak, reversible, and spatially localized noncovalent forces. Such interactions not only prevent catalyst poisoning, but also explain the ease of recovery, and clarify why nanoparticles retain activity even after repeated use. Adsorption energy calculations additionally showed moderate binding strengths and short recovery times, consistent with efficient catalytic turnover without permanent surface occupation.

Although, the results showed that the relatively high nanoparticle loadings were required. This limitation was offset by major operational advantages, including reduced need for pH adjustments, minimized phase contamination, and the potential consolidation of multiple steps into single-vessel processes. Occasional solvent discoloration at elevated temperatures did not compromise the final product, as magnetic separation reliably restored catalyst purity. Overall, the integration of experimental performance with theoretical mechanistic insight establishes these superparamagnetic nanocatalysts as practical, scalable, and mechanistically rational tools for API manufacturing. Their tunable surface chemistry, reversible interaction profiles, and rapid magnetic recovery offer a robust platform for the modern pharmaceutical synthesis, provided that iron content and reaction parameters are appropriately controlled.

Declaration of Interests

A part of this study has been patented in Iranian Patent organization under the Patent No. 110537.

Acknowledgement

The authors are grateful to Mazandaran University of Medical Science, especially the Vice Chancellor of Research, for all kinds of supports for this PhD research project with the grant number 18619.

References

1. a) Research Laboratorium Dr C Janssen. FR1517671, **1961**; b) Research Laboratorium Dr C Janssen. US3141823, **1962**.
2. Jonczyk et al. *Przemysl Chemiczny*, 1978;57:131,133.
3. Suh Y. G., Cho K. H., Shin, D.Y. (**1998**) Total synthesis of fentanyl. Arch. Pharma. Res., 21 (1) 70-72.
4. Richter et al. HU157325, 1970.
5. Ebrahimzadeh M., Babanezhad E., Siadati S. A. (**2025**) Synthetic Routes from 1-(2-phenylethyl)-4-piperidinone (PPD) to Fentanyl; A Short Review, Tabari Biomed. Stu. Res. J., 7 (4) 1-7.
6. Brine A., Boldt J., Huang H., Sawyer J., Carroll D. (**1989**) J Heterocycl Chem., 26 (3) 677–686.
7. Ebrahimzadeh M. A., Siadati S. A., Babanezhad E., Production of fentanyl citrate active pharmaceutical ingredient using superparamagnetic acidic (Fe_3O_4/SiO_2/COOH) and amine ($Fe_3O_4/SiO_2/NH_2$) nanoparticles. Iranian Patent No. 110537. Filed 2023 Sep 6; granted **2024** Feb 1.
8. a) Gupta P. K., Ganesan K., Pande A., Malhotra R. C. (**2005**) J. Chem. Res., (7) 452–453; b) Defence Research Development Organization India. WO2009/116084, **2009**.
9. Valdez CA, Leif RN, Mayer BP. PLoS ONE. 2014;9(9):e108250.

10. Kanamori T., Okada Y., Segawa H., Yamamuro T., Kuwayama K., Tsujikawa K., Iwata Y. T. (**2021**) Biol. Pharm. Bull., 44 (2) 159–161.
11. Walz A. J., Hsu F. L. (**2017**) Org. Prep. Proced. Int. 49 (5) 467–470.
12. Robertson T. B. R., Antonides L.H., Gilbert N., Benjamin S. L., Langley S. K., Munro L. J., Sutcliffe O. B., Mewis R. E. (**2019**) Hyperpolarization of pyridyl fentalogues by signal amplification by reversible exchange (SABRE). Chemistry Open. 8 (12) 1375–1382.
13. Braga F. C., Ramos T. O., Brocksom T. J., De Oliveira K. T. (**2022**) Org. Lett. 24 (45) 8331–8336.
14. Pagliaro M. (**2021**) Catalysis: A unified approach»: A new course in catalysis science and technology. J. Flow Chem., 11 (1) 53-58.
15. Siadati S. A., Ebrahimzadeh M. A., Robati R. Y., Babanezhad E. (**2024**) How to Manufacture a Drug API? A Simple Scheme from synthesis to analysis. Sci. Rad., 3 89-107.
16. Jolliffe H. G., Gerogiorgis D. I. (**2017**) Technoeconomic optimization of a conceptual flowsheet for continuous separation of an analgaesic active pharmaceutical ingredient (API). Industr. Eng. Chem. Res., 56 (15) 4357-4376.
17. Siadati S. A., Soheilizad M., Firoozpour L., Samadi M., Payab M., Bagherpour S., Mousavi, S. M. (**2022**) An Industrial Approach to Production of Tofacitinib Citrate (TFC) as an Anti-COVID-19 Agent: A Joint Experimental and Theoretical Study. J. Chem., 2022 (1) 8759235.
18. Prikeržnik M., Srčič, S. (**2021**) Multivariate analysis for optimization and validation of the industrial tablet-manufacturing process. Drug Develop. Indust. Pharma., 47 (1) 61-71.
19. Dadras A., Rezvanfar M. A., Beheshti A., Naeimi S. S., Siadati S. A. (**2022**) An urgent industrial scheme both for total synthesis, and for pharmaceutical analytical analysis of umifenovir as an anti-viral API for treatment of COVID-19. Comb. Chem. High Throughput Screen., 25 (5) 838-846.
20. a) Kula K., Dobosz J., Jasiński R., Kącka-Zych A., Łapczuk-Krygier A., Mirosław B., Demchuk O. M. (**2020**) [3+ 2] Cycloaddition of diaryldiazomethanes with (E)-3, 3, 3-trichloro-1-nitroprop-1-ene: An experimental, theoretical and structural study. J. Mol. Struct., 1203 127473 b) Siadati S. A., Alinezhad, M. (**2015**) A theoretical study on the functionalisation process of C18NB fullerene through its open [5, 5] cycloaddition with 4-pyridine nitrile oxide. Prog. React. Kinet. Mech., 40 (2) 169-176.
21. Siadati S. A., Davoudi S., Soheilizad M., Firoozpour L., Payab M., Bagherpour S., Kolivand S. (**2023**) The synthesis and the mechanism of a five-membered ring formation between an isothiocyanate and an amide leading to the yield of Enzalutamide anticancer API; a joint experimental and theoretical study. J. Mol. Struct., 1280 (1) 135057.
22. Mazurek A. H., Szeleszczuk Ł., Pisklak D. M. (**2020**) Periodic DFT calculations—review of applications in the pharmaceutical sciences. Pharmaceutics, 12 (5) 415.
23. a) Siadati S. A. (**2016**) A theoretical study on stepwise-And concertedness of the mechanism of 1, 3-Dipolar cycloaddition reaction between tetra amino ethylene and trifluoro methyl azide. Comb. Chem. High Throughput Screen., 19 (2) 170-175; b) Siadati S. A. (**2015**) Effect of steric congestion on the stepwise character and synchronicity of a 1, 3-dipolar reaction of a nitrile ylide and an olefin. J Chem. Res., (39) 640-644.
24. Marinho E. S., Marinho M. M. (**2016**) A DFT study of synthetic drug topiroxostat: MEP, HOMO, LUMO. Int. J. Sci. Eng. Res., 7 (8) 1264.
25. Lamberto D. J., Neuhaus J. (**2021**) Robust process scale-up leveraging design of experiments to map active pharmaceutical ingredient humid drying parameter space. Org. Process Res. Dev., 25 (2) 239-249.
26. Conder E. W., Cosbie A. S., Gaertner J., Hicks W., Huggins S., MacLeod C. S., Remy B., Yang B. S., Engstrom J. D., Lamberto D. J., Papageorgiou C. D. (**2017**) The pharmaceutical drying unit operation: an industry perspective on advancing the science and development approach for scale-up and technology transfer. Org. Process Res. Dev., 21 (3) 420-429.
27. Pradhan B., Mahapatra A. K., Sahu A., Nahak A. (**2024**) Pilot plant scale-up technique of oral solid dosage form in pharmaceutical industry. Res. J. Pharm. Life Sci., 5 (3) 26-59.
28. Meng H., Zhang Z., Zhao F., Qiu T., Yang J. (**2013**) Orthogonal optimization design for preparation of Fe3O4 nanoparticles via chemical coprecipitation. Appl. Surf. Sci., 280 (1) 679-685.
29. Patil S. M., Tandon R., Tandon N. (**2022**) Magnetically recoverable silica-decorated ferromagnetic-nanoceria nanocatalysts and their use with O-and N-butyloxycarbonylation reaction via solvent-free condition. ACS Omega, 7 (28) 24190-24201.
30. Rowley J., Abu-Zahra N. H. (**2019**) Synthesis and characterization of polyethersulfone membranes impregnated with (3-aminopropyltriethoxysilane) APTES-Fe3O4 nanoparticles for As (V) removal from water. J. Environ. Chem. Eng., 7 (1) 102875.
31. Hou S., Li X., Wang H., Wang M., Zhang Y., Chi Y., Zhao Z. (**2017**) Synthesis of core–shell structured magnetic mesoporous silica microspheres with accessible carboxyl functionalized surfaces and radially oriented large mesopores as adsorbents for the removal of heavy metal ions. RSC Adv., 7 (82) 51993-52000.
32. Bahrami M. A., Farhadian N., Karimi M., Forouzan A., Masoumi K. (**2020**) Improvement of pain relief of fentanyl citrate drug encapsulated in nanostructured lipid carrier: Drug formulation, parameter optimization, in vitro and in vivo studies. Drug Des. Devel. Ther., 14 (1) 2033-2045.
33. Pinciroli V., Biancardi R., Visentin G., Rizzo V. (**2004**) The well-characterized synthetic molecule: a role for quantitative 1H NMR. Org. Process Res. Dev., 8 (3) 381-384.

34. Breuker K., Jin M., Han X., Jiang H., McLafferty F. W. (**2011**) Top-down identification and characterization of biomolecules by mass spectrometry. J. Am. Soc. Mass Spectrom., 19 (8) 1045-1053.
35. Ramsay M., Gozdzialski L., Larnder A., Wallace B., Hore D. (**2021**) Fentanyl quantification using portable infrared absorption spectroscopy. A framework for community drug checking. Vib. Spectrosc., 114 (1) 103243.
36. Brettell T. A., Wood M. R. (**2018**) Chromatographic analysis of fentanyl and its analogs. Chromatogr. Tech. Forensic Anal. Des. Drugs, (1) 341-368.
37. Frisch M. J., G. W. Trucks, H. B. Schlegel, G. E. Scuseria, M. A. Robb, J. R. Cheeseman, V. G. Zakrzewski, J. A. Montgomery, R. E. Stratmann, J. C. Burant, S. Dapprich, J. M. Millam, A. D. Daniels, K. N. Kudin, M. C. Strain, O. Farkas, J. Tomasi, V. Barone, M. Cossi, R. Cammi, B. Mennucci, C. Pomelli, C. Adamo, S. Clifford, J. Ochterski, G. A. Petersson, P. Y. Ayala, Q. Cui, K. Morokuma, D. K. Malick, A. D. Rabuck, K. Raghavachari, J. B. Foresman, J. Cioslowski, J. V. Ortiz, B. B. Stefanov, G. Liu, A. Liashenko, P. Piskorz, I. Komaromi, R. Gomperts, R. L. Martin, D. J. Fox, T. Keith, M. A. Al-Lamham, C. Y. Peng, A. Nanayakkara, C. Gonzalez, M. Challacombe, P. M. W. Gill, B. G. Johnson, W. Chen, M. W. Wong, J. L. Andres, M. Head-Gordon, E. S. Replogle and J. A. Pople, Gaussian, Inc., Wallingford CT, Gaussian 03, Revision B.04 Gaussian: Pittsburgh PA, **2003**.
38. Lee C., Yang W., Parr R. G. (**1988**) Development of the Colle-Salvetti correlation-energy formula into a functional of the electron density. Phys. Rev. B, 37 (1) 785-789.
39. Delchev V. B., Nenkova M. V. (**2008**) Theoretical modeling of the ground state intramolecular proton transfer in cytosine: DFT level study. Acta Chim. Slov., 55 (1) 132-137.
40. Costa A. C., Ondar G. F., Versiane O., Ramos J. M., Santos T. G., Martin A. A., Raniero L., Bussi G. G. A., Téllez Soto C. A. (**2013**) DFT: B3LYP/6-311G (d, p) vibrational analysis of bis-(diethyldithiocarbamate)zinc (II) and natural bond orbitals. Spectrochim. Acta A Mol. Biomol. Spectrosc., 105 (1) 251-258.
41. Hamidallah K., Zourif A., Kouniba S., Safi Z., Bensalah J., Benbiyi A., Guendouzi M. E., Anouar A. (**2024**) Insights of the adsorption mechanism of Bemacid Red using coagulation-flocculation sludge: Optimisation using BBD-RSM and DFT calculations. J. Mol. Liq., 409 (1) 125540.
42. Sakarya A., Dalgic S., Dalgic S. S. (**2021**) Comparison of the stability of 2H nanosurfaces by the adsorption of small molecules: A DFT study. Int. J. Sci. Res. Sci. Technol., 8 (6) 122-129.
43. Lu T., Chen F. (**2012**) Multiwfn: a multifunctional wave function analyzer. J. Comput. Chem., 33 (5) 580-592.
44. Williams T., Kelley C. (**2011**) Gnuplot 4.5: an interactive plotting program. URL http://gnuplot.info; b) Wang J., Ferguson A. L. (**2016**) Nonlinear reconstruction of single-molecule free-energy surfaces from univariate time series. Phys. Rev. E, 93 (3) 032412.
45. Thomas W, Kelley C (**2011**) Gnuplot 4.5: an interactive plotting program. http://gnuplot.info. Accessed Oct 2023 17. Humphrey W, Dalke A, Schulten K (**1996**) VMD: visual molecular dynamics. J. Mol. Graphics 14 (1) 33–38. https:// doi. org/ 10. 1016/0263-7855(96)00018-5.
46. Yang K., Peng H., Wen Y., Li N. (**2010**) Re-examination of characteristic FTIR spectrum of secondary layer in bilayer oleic acid-coated Fe_3O_4 nanoparticles. App. sur. sci., 256 (10) 3093-7.
47. Khabibullin V. R., Chetyrkina M. R., Obydennyy S. I., Maksimov S. V., Stepanov G. V., Shtykov S. N. (**2023**) Study on doxorubicin loading on differently functionalized iron oxide nanoparticles: implications for controlled drug-delivery application. Int. J. Mol. Sci., 24 (5) 4480.
48. Wang Z., Zhou C., Xia J., Via B., Xia Y., Zhang F., Li Y., Xia L. (**2013**) Fabrication and characterization of a triple functionalization of graphene oxide with Fe3O4, folic acid and doxorubicin as dual-targeted drug nanocarrier. Colloids and surfaces B: biointerfaces., 106 (1) 60-65.
49. Ali M., Ali S. R., Amir S. S., Ali A. T. S. (**2016**) Synthesis and application of highly active dithiooxamide functionalised multi-walled carbon nanotubes toward mercury removal from aqueous solution. Pakistan Journal of Scientific & Industrial Research Series A: Phys. Sci., 59 (1) 23-29.
50. Rauf A., Ahmad Z., Ajaj R., Zhang H., Ibrahim M., Muhammad N., Al-Awthan Y. S., Bahattab O. S., Ullah I. (**2025**) Green synthesis an eco-friendly route for the synthesis of iron oxide nanoparticles using aqueous extract of Thevetia peruviana and their biological activities. Sci. Rep., 26 (1) 18316.

© 2026 by the authors; licensee Growing Science, Canada. This is an open access article distributed under the terms and conditions of the Creative Commons Attribution (CC-BY) license (http://creativecommons.org/licenses/by/4.0/).